

# SCIENTIFIC REPORTS



OPEN

## The nature of photoinduced phase transition and metastable states in vanadium dioxide

Received: 27 September 2016  
Accepted: 10 November 2016  
Published: 16 December 2016

Zhensheng Tao<sup>1,†</sup>, Faran Zhou<sup>1</sup>, Tzong-Ru T. Han<sup>1</sup>, David Torres<sup>2</sup>, Tongyu Wang<sup>2</sup>, Nelson Sepulveda<sup>2</sup>, Kiseok Chang<sup>1</sup>, Margaret Young<sup>3</sup>, Richard R. Lunt<sup>1,3</sup> & Chong-Yu Ruan<sup>1</sup>

Photoinduced threshold switching processes that lead to bistability and the formation of metastable phases in photoinduced phase transition of VO<sub>2</sub> are elucidated through ultrafast electron diffraction and diffusive scattering techniques with varying excitation wavelengths. We uncover two distinct regimes of the dynamical phase change: a nearly instantaneous crossover into an intermediate state and its decay led by lattice instabilities over 10 ps timescales. The structure of this intermediate state is identified to be monoclinic, but more akin to M<sub>2</sub> rather than M<sub>1</sub> based on structure refinements. The extinction of all major monoclinic features within just a few picoseconds at the above-threshold-level (~20%) photoexcitations and the distinct dynamics in diffusive scattering that represents medium-range atomic fluctuations at two photon wavelengths strongly suggest a density-driven and nonthermal pathway for the initial process of the photoinduced phase transition. These results highlight the critical roles of electron correlations and lattice instabilities in driving and controlling phase transformations far from equilibrium.

Phase transitions are often discussed within the context of thermal equilibrium where distinct phase change phenomena are described in the complex phase diagram in which temperature, chemical doping, or pressure are steady-state tuning parameters. Much less is understood in terms of excited states and dynamical phase transitions induced after sudden excitations using intense laser pulses<sup>1,2</sup>. In this strongly nonequilibrium condition, the thermodynamic ground state may become less stable than its counterparts and metastable new phases may emerge<sup>3,4</sup>. Characterizing the nonequilibrium transformations between two thermodynamic phases directly or through a metastable phase indirectly may provide valuable insights regarding the nature of these states, the interactions, and the active coordinates involved in these phase transitions<sup>5</sup>.

As a prime example of phase transitions, the metal-to-insulator transition in VO<sub>2</sub> has attracted wide-spread attention and is one of the best studied at the ground states near equilibrium. Pristine VO<sub>2</sub> crystals undergo a first-order transition from a high-temperature metallic phase with a rutile (R) structure to a low-temperature insulating phase with a monoclinic (M<sub>1</sub>) structure at the transition temperature  $T_c = 340 \text{ K}^{6-8}$ . The introduction of electron<sup>9</sup> and hole<sup>10</sup> doping changes the transition temperature, as well as leads to the appearance of new phases such as M<sub>2</sub> and T, resulting in a complex phase diagram as illustrated in Fig. 1(a). To decipher the apparent synergy between the electronic and lattice degrees of freedom culminating to a large-scale electronic switching<sup>11,12</sup>, scenarios involving both Mott-Hubbard<sup>10,13</sup> and Peierls<sup>14,15</sup> physics were proposed, and their verifications have been the subjects of intense experimental investigation, particularly using ultrafast pump-probe approaches<sup>15-22</sup> to transiently isolate the active components.

Among the established work, ultrafast insulator-metal transition (IMT) has been the early focus using ultrafast optical pump-probe techniques. A view based on the temporal hierarchy suggested a nonequilibrium nature of transformations, judged from the ~100 fs timescale optical responses<sup>22-24</sup> and x-ray absorption changes<sup>25</sup>, which clearly is decoupled from the structural transitions expected to proceed on ps electron-phonon coupling or longer timescale. This ultrashort temporal response in optical properties may reflect the differences in heat capacity in electronic and lattice degrees of freedom, thus yielding different response times in suppressing the

<sup>1</sup>Department of Physics and Astronomy, Michigan State University, East Lansing, Michigan 48824 USA. <sup>2</sup>Department of Electrical and Computer Engineering, Michigan State University, East Lansing, Michigan 48824 USA. <sup>3</sup>Department of Chemical Engineering and Materials Science, Michigan State University, East Lansing, Michigan 48824 USA. <sup>†</sup>Present address: Department of Physics and JILA, University of Colorado and NIST, Boulder, Colorado 80309, United States. Correspondence and requests for materials should be addressed to C.-Y.R. (email: ruan@pa.msu.edu)

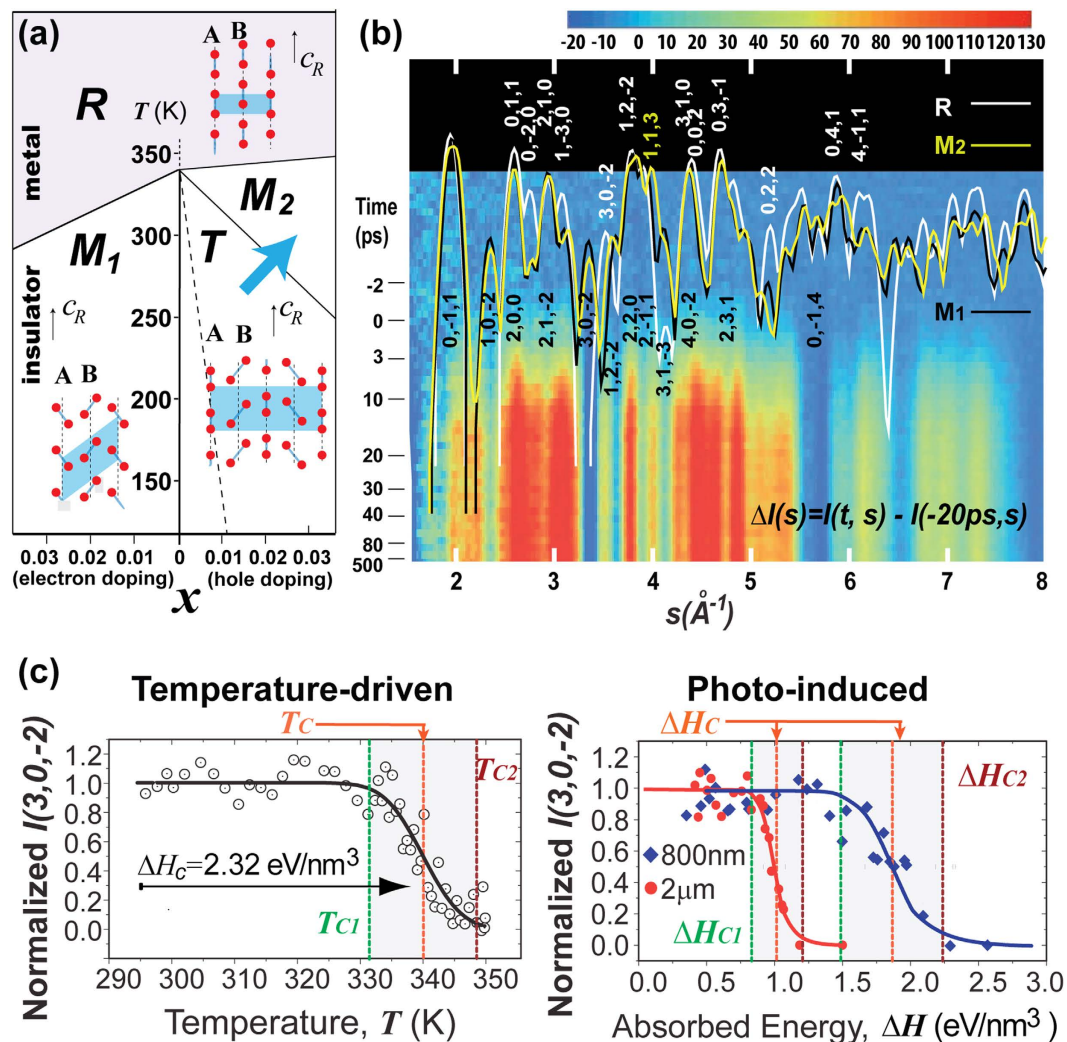


**Figure 1. Phase transitions of VO<sub>2</sub>.** (a) Layout of the phase diagram of VO<sub>2</sub>, along with the schematic diagram of structural displacements in each phase. (b) The time-dependent diffraction curves from VO<sub>2</sub> films driven by 800 nm pulses, presented in difference map (reference -20 ps). The simulated diffraction curves, in log scale along with the corresponding Miller indices, based on known crystalline phases are overlaid atop the difference map for comparison. (c) The M<sub>1</sub>-to-R transition curves under the steady-state heating (black) and under excitations of near-IR (800 nm, blue) pulses, mid-IR (2000 nm, red) pulses. The solid curves are error function fittings to derive the critical energy density  $\Delta H_c$  and transition window specified by  $\Delta H_c \pm 2\sigma$ . The initial sample temperature is 294 K.

respective order parameters (optical gap and diffraction intensity) through coupling between transiently isolated sub-systems<sup>26,27</sup>. However, through pump-fluence dependent studies, the evidences of decoupling on the long-range scale between electronic and structural phases were demonstrated in the observation of a threshold for the onset of IMT to be  $\leq 1 \text{ mJ/cm}^2$ <sup>20,24</sup>, in distinct contrast to the onset fluence of 4–8  $\text{mJ/cm}^2$ , identified for the monoclinic-to-rutile structural changes using electron<sup>16,27,28</sup> and x-ray<sup>17</sup> diffraction or from persistent THz conductivity<sup>20,21</sup>. From the viewpoint of displacive excitation of coherent phonons<sup>29</sup>, the interplay between the electronic and lattice degrees of freedom were examined. Notably, structural bottleneck in IMT is proposed based on a minimum transition time of  $\sim 75 \text{ fs}$ , which corresponds to one-half period of the  $A_g$  phonon modes that stretch and twist the V-V dimers as the active modes driving the electronic changes<sup>15</sup>. More detailed classification of the modes<sup>18,20,30</sup> and their role as active modes pertaining to insulating or metallic phase<sup>30</sup>, as well as emerging anisotropy near critical temperature<sup>26</sup>, were reported, suggesting the involvements of different phonon modes during the phase transitions. In particular, two distinct symmetry changes involving the initial steps of monoclinic-to-rutile transformation were identified through ultrafast electron diffraction<sup>16,28</sup>. Meanwhile, in the strongly driven regime, a sub-60 fs band-gap collapse breaking the structural bottleneck timescale was demonstrated in ultrafast photoemission studies, implying the dominant energy scale at the Fermi energy being the electron correlations<sup>22,31</sup>. Given the temporal hierarchy and the distinct thresholds between the electronic and structural transitions, a new monoclinic metallic phase that bridges the two transition has been suggested<sup>18,27</sup> and their presence as a long-lived metastable state induced under photoexcitations<sup>28,32,33</sup>, or induced under strong

stress<sup>34,35</sup> and/or carrier doping<sup>27,35</sup> were increasingly reported. Identifying the emergence of such a new state and clarifying its role in mediating the electronic and structural transformations are of major interests to address key open questions regarding the apparent complexities involved in the phase transition of VO<sub>2</sub>.

In this work, we present controlled studies to examine the transient emergence of new metastable phases and their nonequilibrium dynamics during photoinduced phase transitions of VO<sub>2</sub> using femtosecond electron diffraction<sup>16,36,37</sup> and diffusive scattering techniques, which allow us to directly monitor the momentum-dependent lattice dynamics. With different wavelengths of optical pumping, we demonstrate that the photoinduced phase transitions in VO<sub>2</sub> is non-thermal, evidenced by the fact that the optical threshold of the phase transition is best described in terms of photodoping rather than the energy density. By investigating the transient diffraction patterns, we discover a unique interaction-driven monoclinic emergent state that, interestingly, has a similar crystal symmetry as the thermodynamic M<sub>2</sub> phase. Our results show that the photoinduced phase switching between the insulating M<sub>1</sub> and the metallic R phases can be significantly more efficient by accessing the intermediate phase and the new correlation-driven pathways.

## Results and Discussion

In our experiments, we employed ultrafine films of VO<sub>2</sub> nanocrystalline grains (size  $31 \pm 7$  nm) prepared on a 9 nm amorphous Si membrane using vapor deposition method (see Methods). The grain size and nano-film settings were chosen to leverage their flexibility on the nanometer scale to avoid excessive stress<sup>27,38</sup> that may otherwise develop during disruptive structural transitions. These samples display high crystallinity from clear crystalline powder diffraction (see Supplementary Fig. S1). Using the ultrafast electron diffraction setup<sup>5</sup> (see Methods), the patterns of time-dependent diffraction are recorded in the difference map in Fig. 1(b), where the patterns from different known VO<sub>2</sub> crystalline phases<sup>39–41</sup> are also shown. Sufficiently low repetition rates ( $\leq 500$  Hz) were employed to avoid irreversible changes [see Supplementary Information (SI) for details]. The major sequence of events associated with symmetry-recovery phase transition from M<sub>1</sub> to R can be identified based on the evolution of relative Bragg intensities. Such evolution is sensitive to changes in the two critical lattice distortions (pairing and twisting) along the V-V sub-lattice chains (A and B), as depicted in Fig. 1(a). For example, the ultrafast transformation of the distorted M<sub>1</sub> is measured by diminishing pairing-specific reflections [e.g. (3, 0, -2), (1, 0, -2), (3, 1, -3)] in the early transition, whereas at the later times formation of the undistorted R is confirmed from specific enhancements and movements of the high-symmetry peaks.

Our controlled studies were based on femtosecond (45 fs) infrared (IR) pumping using two different photon wavelengths, 800 nm and 2  $\mu$ m (photon energy  $E_\lambda = 1.55$  and 0.62 eV respectively), through which different energy densities were absorbed by the VO<sub>2</sub> crystals to produce a similar number of electron-hole pairs. The transition curves presented in Fig. 1(c) were obtained by incrementally increasing the laser fluence while observing the intensity of order-parameter reflection (3, 0, -2) at +150 ps delay. Indeed, using near-IR (800 nm) pump pulses we observed clear threshold switching behavior with the transition at a critical fluence  $F_C \sim 7$  mJ/cm<sup>2</sup> (determined by fitting with the error function) at room temperature. This is within the range of previously identified thresholds (4–8 mJ/cm<sup>2</sup>) also under 800 nm photoexcitation<sup>16,19,20,22,27,28,30,31</sup>. We note that in order to precisely determine the pump-laser fluence, we measure the pump-laser spot size *in situ* by the knife-edge and laser-electron cross-correlation measurements (see Methods and SI). The error of fluence measurements introduced by laser-spot size measurements is no more than 25%. To compare with thermal transition, the absorbed optical energy density  $\Delta H$  is calculated from the applied fluence  $F$  by  $\Delta H = F\gamma/d$ , where  $d$  is the film thickness. The absorption coefficient  $\gamma$  is carefully determined through measuring the wavelength-dependent transmittance and reflectance using the transfer matrix method on the as-grown VO<sub>2</sub> films (see SI for details). Based on  $F_C$ , the critical energy dose  $\Delta H_C$  for 800 nm pump is  $\sim 2$  eV/nm<sup>3</sup> which is close to the thermal requirement (2.32 eV/nm<sup>3</sup>) for transition between M<sub>1</sub> and R<sup>42</sup>, calculated based on integrating heat capacity and latent heat (see SI for details). This similarity between  $\Delta H_C$  estimated from photoinduced and thermal transitions has been the reason behind considering the near-IR-driven phase transition as quasi-thermal in the established work. However, we show that the mid-IR (2  $\mu$ m) pumping leads to a much smaller critical dose ( $\Delta H_C \sim 1$  eV/nm<sup>3</sup>). This unexpected result is demonstrated over a range of temperatures [Fig. 2(a)], where we consistently observe a subthermal critical dose under mid-IR whereas the transition under near-IR occurs close to the thermal threshold. However, this disparity may be reconciled by converting the critical energy density to the absorbed photon density  $n_C = \Delta H_C/E_\lambda$  depicted in Fig. 2(b). The critical lines separating M<sub>1</sub> and R as defined by  $n_C$  determined using the two optical excitations then agree quite well. This result thus indicates that the fundamental process of photoinduced phase transitions is very different from a thermally induced transition, and strongly suggests a density-driven mechanism at play in the photoinduced phase transition between M<sub>1</sub> and R phases<sup>1</sup>.

We note that our results are distinctly different from the conclusions drawn in ref. 24, which we believe can be attributed to the difference in experimental approaches. In ref. 24, the optical response shortly after pump excitation (+200 fs) was monitored leading to the reported thresholds of the absorbed energy density several times smaller than our results and other work<sup>16,18–21,28,30</sup>. Indeed, as shown in previous THz spectroscopy studies<sup>18–21</sup>, even though the optical conductivity is increased by laser-induced photodoping in  $\sim 100$  fs, such increment decays within 1 ps so that it does not persist to induce a full phase transition in VO<sub>2</sub>. In our experiments, however, we monitor the VO<sub>2</sub> structure at a time well after pump laser excitation (+150 ps) in order to observe the threshold of the full photoinduced phase transitions.

The discovery that the mid-IR-driven structural transformation is significantly subthermal has direct ramifications in understanding the unconventional features of photoinduced phase transitions in VO<sub>2</sub>. In particular, the fact that  $\Delta H_C$  required for driving transition from M<sub>1</sub> to R by pumping VO<sub>2</sub> with the mid-IR photons is even below the thermal latent heat (1.47 eV/nm<sup>3</sup>)<sup>42,43</sup> [Fig. 2(a)] suggests a very different pathway that does not involve significant entropy and that may be facilitated by strongly interacting electrons similar to the pathway of chemical doping as elucidated by the phase diagram [Fig. 1(a)]. In such a scenario, the photoexcitation explores excited

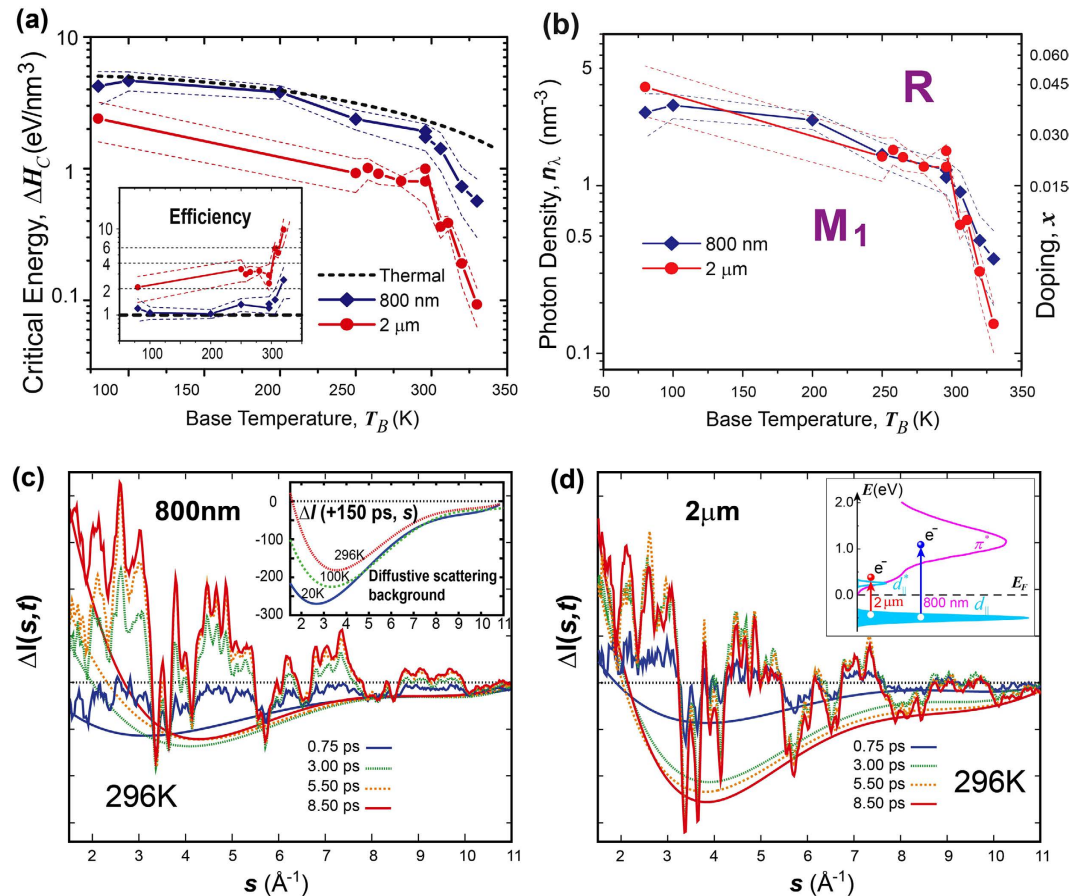


**Figure 2. Phase transitions of VO<sub>2</sub> under optical pumping.** (a) The transition critical energy density,  $\Delta H_C$  (solid) and  $\Delta H_C \pm \sigma$  (dash), as a function of crystal temperature  $T_B$  under two different optical excitations. The thermal critical threshold (dash, black) is also plotted for comparison. The inset in (a) shows the efficiency based on normalizing the  $\Delta H_C$  associated with the photoinduced transitions obtained for each  $T_B$  with the corresponding  $\Delta H_C$  from the thermal transition. (b) The optical doping – temperature phase diagram, converted from (a), where the photon density  $n = \Delta H/E_\lambda$ , the doping  $x = n \cdot V_R$ , and the VO<sub>2</sub> formula volume  $V_R = 2.96 \times 10^{-23} \text{ cm}^3$ . (c,d) The diffraction difference curves  $\Delta I(s, t)$  obtained by subtracting the reference ground state curve ( $-20 \text{ ps}$ ) from the time-dependent diffraction curve  $I(s, t)$ . To highlight the trend of the diffusive scattering evolution, curves are obtained by fitting the baseline line using a 4<sup>th</sup> order polynomial function via maximizing the non-negativeness of  $\Delta I(s, t)$  (see text). The inset in (c) shows the temperature-dependent diffusive scattering curves obtained at 150 ps. The inset in (d) illustrates the interband transitions induced by 800 nm and 2 μm pump lasers from the  $d_{||}$  band to the  $\pi^*$  band of VO<sub>2</sub>. The density of states qualitatively reproduce the results in ref. 11.

energy landscape with new emergent properties as defined by a reconstructed energy landscape induced by photodoping, which are not the same as those pertaining to the temperature-driven phases<sup>3–5</sup>. Nonetheless, thus far, the understanding of the emergent state properties focuses on the effect of photodoping, whereas the frequently used near-IR pulses ( $E_\lambda = 1.55 \text{ eV}$ ) not only excite charge carriers that promptly induce doping of correlated electron orbitals, but also impart their excessive photon energy ( $\Delta = E_\lambda - E_g$ ,  $E_g = 0.6 \text{ eV}$  is the optical gap<sup>44,45</sup>) which can translate to the lattice as stochastic heating at a timescale of 10 ps and longer. The application of mid-IR pulses (0.62 eV) thus represent an important test scenario where at the same level of charge carrier excitation, their initial excessive photon energy is reduced by nearly an order of magnitude compared to near-IR excitations. To carefully evaluate the impact of both doping and thermal effects, we resort to directly observing the details of the nonequilibrium dynamics under two different photon wavelengths. To follow the coherent structural evolution driven by the sudden electronic impact, we examine the time-dependent coherent Bragg diffraction. Meanwhile, to gauge the role of lattice instabilities and thermal fluctuations we monitor the diffusive scattering away from the Bragg peaks.

Given the short wavelength of the electron beam, the large Ewald sphere associated with ultrafast electron diffraction experiments provides an easy access to short and long-range scale dynamics manifested in both Bragg diffraction and diffusive scattering channels in the reciprocal space that are simultaneously recorded with an area detector. First, we examine the lattice structural evolution during VO<sub>2</sub> phase transition, where the critical lattice distortions (pairing and twisting) along the chains A and B [Fig. 1(a)] are at the level of 7% of the

interatomic V-V distance ( $\sim 2.8 \text{ \AA}$ ) or less. These subtle changes lead to only a few percent adjustments of key Bragg peak intensities and are best described in the diffraction difference curve  $\Delta I(s, t)$  at different pump-probe time delays ( $t$ ) as depicted in Fig. 2(c) and (d). Here,  $\Delta I(s, t) = I(s, t) - I(s, t < 0)$ , where  $I(s, t)$  is the 1D scattering wave-vector ( $s$ )-dependent pattern reduced by radially averaging the 2D powder diffraction patterns as shown in the Supplementary Fig. S2(b). We note Fig. 2(c) and (d) are obtained using two different pump lasers (800 nm and  $2 \mu\text{m}$ ) set at the upper density threshold [ $n_{c2} = \Delta Hc_2/E_\lambda$ , see Fig. 1(c)], but differing in energy density delivered to  $\text{VO}_2$  nanocrystals. It is intriguing to see that despite of very different excess energy imparted in  $\text{VO}_2$  crystals, the ultrafast timescale relative changes in the Bragg diffraction show nearly synchronous evolution between the near-IR and mid-IR excitations. These ultrafast cooperative evolutions feature the suppression of pairing-specific peaks and the transfer of scattering weight to higher symmetric peaks. These processes describe a transition from  $M_1$  to a new state with lower lattice distortions being induced by carrier excitations rather than heating.

Next, we turn our attention to the evolution of diffusive scattering (DS) in the region between the Bragg peaks. In the steady-state investigation, DS has traditionally been the source of information for probing the lattice fluctuations and inhomogeneous strain<sup>46</sup>, and in the case of 2D diffraction from nanocrystals, such signals are isotropically integrated, forming a smooth background underneath the Bragg peaks. In ultrafast diffraction, the time-independent common background of  $I(s, t < 0)$ , predominantly consisted of incoherent features such as the atomic background and elastic scattering from atomic impurities, are effectively removed in  $\Delta I(s, t)$ . Therefore, the observed background changes represent the photoinduced features, including inelastic phonon scattering and inhomogeneous strain that evolves as a function of time after pump-laser excitation. Two distinctive dynamics differentiated by their momentum transfer ( $s$ ) and timescale are observed. First, in proximity to the Bragg peaks, the diffusive background exhibits sub-ps suppression. This feature correlates well with an ultrafast shift in the bonding state featured also in the recovery of local symmetry witnessed earlier in the Bragg diffraction on a similar timescale. Here, the suppression of DS represents a reduction of non-uniform strain present in nanocrystals, as part of global symmetry recovery dynamics. Meanwhile, we observe an increase of DS at the small  $s$  (in regions below the coherent Bragg diffraction) that continues over ps timescales. This enhanced DS at small  $s$  signifies the emergence of unique longer wavelength correlations, which is highly dependent on the excitation wavelength. We can correlate the contrasting long-wavelength DS in Fig. 2(c) and (d), drawn on the same relative scale, with the different applied photon excess energies. Much larger increase is seen on  $\sim 10$  ps timescale under 800 nm excitation than under  $2 \mu\text{m}$  excitation. The correlation between such DS and crystal temperature can also be established from the temperature-dependent studies [see inset of Fig. 2(c)], where such an enhancement is reduced at lower temperature under the same optical dose ( $\Delta n_{c2}$ ) over a longer time (+150 ps). Note, to guild the eyes, the overall trend of DS can be followed through the curves underneath the  $\Delta I(s, t)$ , and those presented for the temperature-dependent studies, generated through a 4<sup>th</sup> order polynomial fit of  $\Delta I(s, t)$  via optimizing the non-negativeness – a practice also used in isolating the incoherent scattering background contribution in powder diffraction curves<sup>47,48</sup>. The fact that a significantly lower level of lattice instabilities was found when the mid-IR pump was applied compared to the near-IR one suggests a much lower energy dose being transferred to the lattice. These clear wavelength-dependent results support that the initial photoinduced phase transition is indeed nonthermal.

To further identify the density-driven state featured by the coherent structural evolution, we examine the transient evolution of the intensity and position of phase-sensitive Bragg peaks over  $s = 3.5$  to  $4.5 \text{ \AA}^{-1}$  (Fig. 3). These changes are monitored in reference to the initial ( $M_1$ ) and final (R) state parameters both in the longer [Fig. 3(a)] and in the ultrafast [Fig. 3(b)] timescales. Judging from the Bragg peak intensity changes [(4, 0, -2) and (2, 2, 0)/(2, -1, 1) in Fig. 3(a)], we find that the transition into a metastable phase, which is neither  $M_1$  nor R, is established following initial cooperative structural evolutions (stages I & II, to be discussed later), as further detailed in Fig. 3(b) along with several other reflections. The metastable phase starts its relaxation into R at a well-defined onset time  $\sim 15$  ps as characterized by a sharp drop of (4, 0, -2) and (2, 2, 0)/(2, -1, 1) intensity (stage IV) as depicted in Fig. 3(c). But the changes are different over two different excitations, in particular with regard to generation of acoustic oscillations that are seen in the modulation of the Bragg intensities. Scenarios to a stable excited electronic manifold due to the soft-band effect in the narrow-gap Mott insulator  $\text{VO}_2$  have recently been proposed theoretically<sup>49</sup>. In our experiments, the above-the-gap photoexcitations inject electrons into the spatially extended  $\pi^*$  ( $V3d\text{-}O2p$ ), and leave holes in the localized spin-singlet  $d_{||}$  ( $V3d\text{-}V3d$ ) orbitals (see inset of Fig. 2(d))<sup>8,11</sup>, effectively prompting hole doping. Given the spatially decoupled orbital symmetry between these states that weakens excitonic coupling<sup>50</sup>, the long-lived excited charge carriers can drive ps timescale structural evolution into a new state which is a local minimum in the excited energy landscape. Furthermore, given the strongly interacting nature<sup>44,51</sup> the evolution may proceed beyond the rigid-band picture<sup>11,12</sup>, and establish a new metastable state. This correlation-driven dynamics for reconstructing the electronic energy landscape can be reconciled with the density-driven characteristics as witnessed here, and more specifically the relevant energy scale for triggering the phase transition is set by the hole doping concentration defining the well-established threshold behavior<sup>5</sup>. Meanwhile, with the elevated transient photo-carrier concentration (up to  $\sim 10^{21} \text{ cm}^{-3}$ ) the emergent state could exhibit metallic transmissivity<sup>28</sup> and THz conductivity<sup>18,20</sup>, despite that it is not in a true metallic ground state.

According to our results shown in Fig. 3, there appears to be no direct pathway connecting  $M_1$  to R over the excited landscape in the density-driven regime. The cooperative structural evolutions into the metastable phase presented here were obtained at the same doping level  $n_{c2}$ , which is  $\sim 20\%$  above the mean threshold of the transition. Meanwhile, an excitation-wavelength-dependent contrasting build-up of the long-wavelength diffusive scattering [Fig. 3(c)] on the timescale of the decay reflects the different applied photon energies translating into lattice instabilities. The relaxation of the emergent state, which, according to its correlation to the diffusive scattering changes, can be associated with instability-driven decay of charge carriers. The process is disruptive enough to initiate strain waves manifested in the breathing mode of  $\text{VO}_2$  nanograins, as observed in the oscillations of

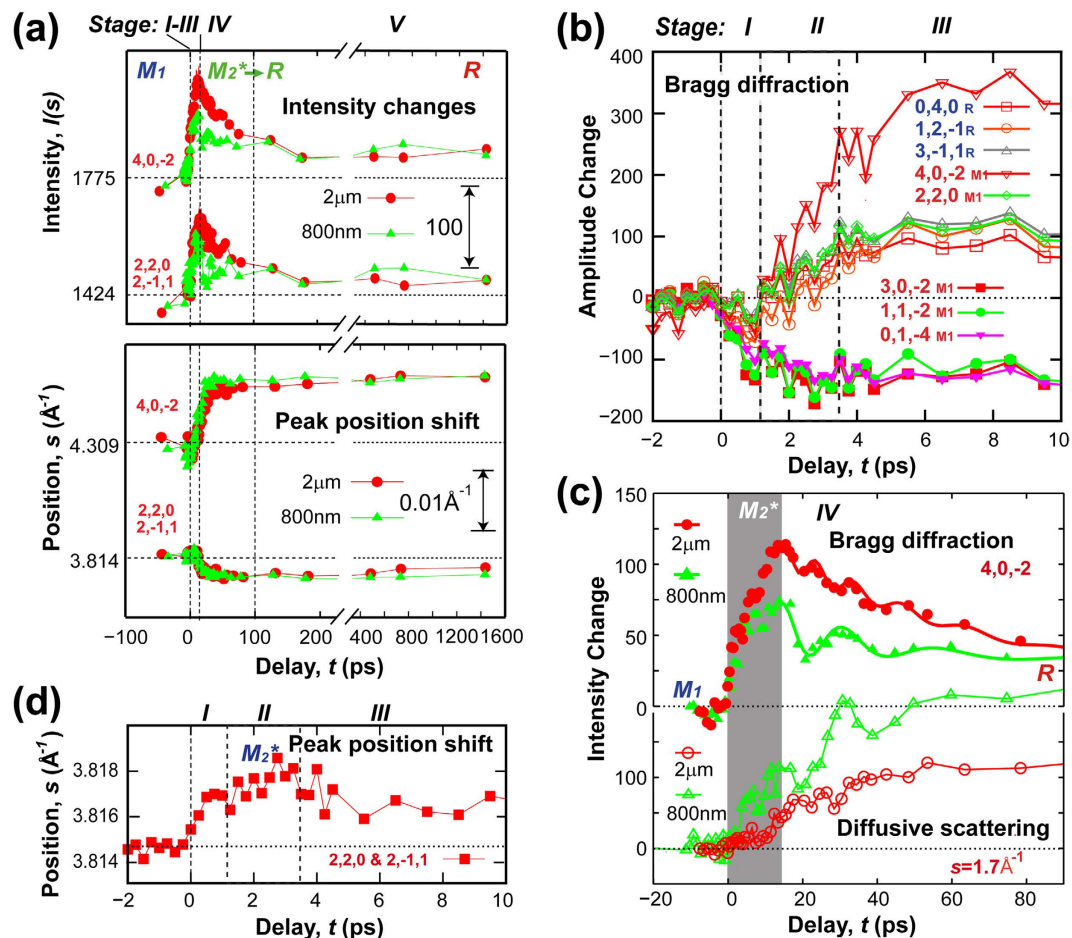


**Figure 3. Ultrafast evolutions of Bragg diffraction and diffusive scattering.** (a) The intensity and position evolutions of the selected Bragg peaks during structural phase transition from  $M_1$  to R. The laser doses for two different excitations (800 nm and 2  $\mu\text{m}$ ) are set to  $n_{e2} \sim 1.85 \text{ nm}^{-3}$ , which is above the transition critical dose ( $n_c = 1.25 \text{ nm}^{-3}$ ) at crystal temperature  $T_b = 294 \text{ K}$ . (b) The scale-up view of the transitions for the first 10 ps, during the formation of metastable phase  $M_2^*$ , under 800 nm excitation, including both low-symmetry pairing specific and higher-symmetry reflections. (c) The scale-up view of the transitions in the intermediate timescale where the decay of metastable phase occurs. The evolution of diffusive scattering amplitude monitored at  $s = 1.7 \text{\AA}^{-1}$  are also depicted for comparison. (d) Scale-up view of the center-of-mass position evolution of the  $(2, 2, 0)$  &  $(2, -1, 1)$  diffraction groups.

the diffraction intensity in Fig. 3(c). The oscillations are more pronounced when driven by the near-IR photons, which also leads to a shorter decay time (6 ps), as compared to the mid-IR pump (40 ps). The timescales are fitted with a function of exponential decay modulated by chirped harmonic oscillations. The oscillation period shifts from  $\sim 13$  ps at the onset to  $\sim 25$  ps near the end of each decay, suggesting a varying sound speed from 4.5 km/s to 2.5 km/s (based on breathing mode over  $\sim 30$  nm grains). It is worth to mention that the lattice softening leading to a similar change of the sound velocity during monoclinic-to-rutile phase transition was also observed previously<sup>52</sup>. Given that the supporting ultrathin Si film for growing the  $\text{VO}_2$  is amorphous, it is expected that the sample-substrate strain mismatch as shown in previous work<sup>34</sup> does not contribute to our results. Therefore, we expect the evolution of the strain is intrinsic to the  $\text{VO}_2$  nanocrystal induced during phase transitions. It is also worth noting that the onset of the transition correlates well with a build-up of long-wavelength fluctuations near unitcell distance or longer ( $\sim 2\pi/s_c$ ,  $s_c \geq 1.7 \text{\AA}^{-1}$ ) revealed in the diffusive scattering [Fig. 3(c)], suggesting median range lattice fluctuations to be effective in facilitating carrier relaxations.

The energy-dependent nonequilibrium dynamics reported here elucidate the exceptional nature of the density-driven photoinduced phase transitions in  $\text{VO}_2$ , which may be similar to the photoinduced insulator-metal transition involving charge-density wave transformation in  $\text{TaS}_2$ <sup>5</sup>. In particular, the density-driven emergent state offers a new pathway to reach a stable R phase by circumventing the energy and time consuming entropic barrier. Regarding the identity of the emergent state, we conduct structure analysis based on the integrated intensity evolution leading to such a phase, as depicted in Fig. 4(a) [compared to Fig. 3(b), the intensity is integrated over the Bragg peak envelop after removing the scattering background]. The transition shown in the evolution of  $(2, 2, 0)$ ,  $(2, 3, 1)$  and  $(4, 0, -2)$  intensities over stages I&II indicates separate steps of lattice relaxations. The suppression up to 70% of  $(3, 0, -2)$ ,  $(3, 1, -3)$  intensities is the dominant feature during stage I, which indicates a de-pairing

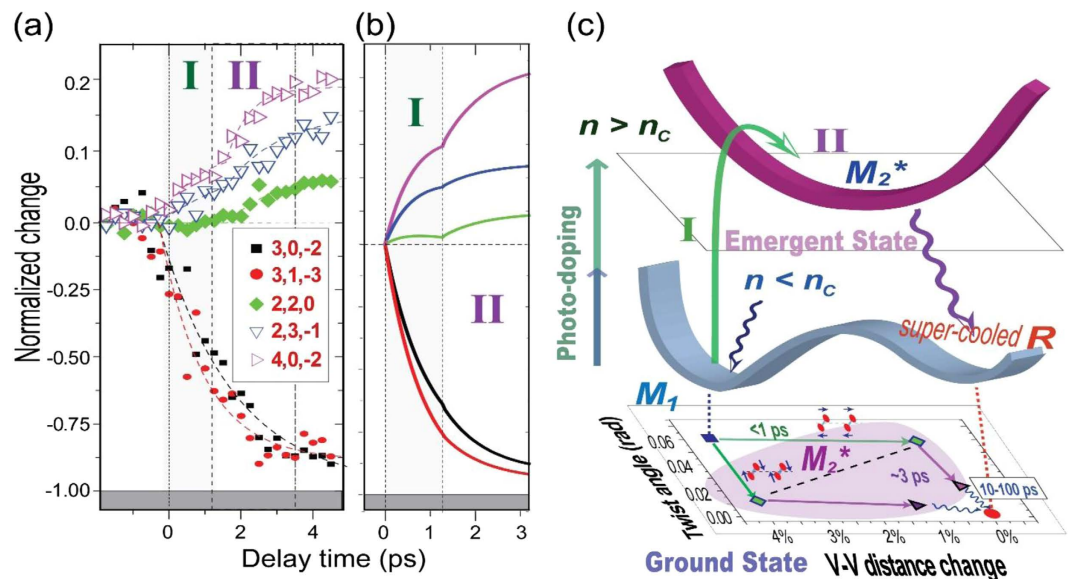


**Figure 4. Ultrafast transformation pathways of VO<sub>2</sub>.** (a) The integrated intensity changes based on the data presented in Fig. 3 (with diffusive background subtraction) under 800 nm excitation. The dashed lines are drawn as a guide to the eyes. (b) Simulated intensity changes based on a two-step transition model along the pathways to reduce the lattice distortions along two critical modes [coordinates depicted in (c)]: (I) from  $M_1$  to  $M_2^*$  (transition state), and (II) from  $M_2^*$  towards R. (c) Conceptual depiction of interaction energy landscape in the multistep phase evolutions along with a plot depicting the corresponding time steps and changes along de-pairing and detwisting coordinates estimated from the experimental data.

process based on symmetry argument. Meanwhile, changes over higher symmetry reflections along different planes are also observed, suggesting a three-dimensional structural changes. With the lattice parameters frozen, we conduct analyses on the initial different structural transformations directed along the two critical structural modes (pairing and twisting) on the A and B sub-lattice chains.

We find that processes in stages I&II depicted in the diffraction intensity evolution [Fig. 4(a)] can be emulated through a pathway in which  $M_2^*$  (\*denotes nonequilibrium, excited nature) serves as a metastable intermediate structural motif, where half of the chains are unpaired, while the other half are untwisted, as shown in Fig. 4(b) [skeleton evolution depicted in Fig. 4(c)]. In contrast, simultaneously or sequentially reducing the pairing and twisting of both sublattice chains cannot capture the key features of the experimental data (see SI for details). From the perspective of crystalline state evolution, the initial switchover to  $M_2^*$  is also identified from the appearance of  $M_2$  (1, 1, 3) reflection (representing unitcell doubling in the basal plane) near  $s = 4 \text{ \AA}^{-1}$  as shown in Fig. 1(b). The transition into this new motif and its relaxation can be analyzed from monitoring the center-of-mass evolution of the reflection group containing the  $M_2$ -specific reflection and nearby monoclinic (2, 2, 0) and (2, -1, 1) reflections in total diffraction. As shown in Fig. 3(d), the center-of-mass position initially moves toward strengthening the  $M_2$  characters, opposite to what would occur if the structure directly evolves into R, which occurs only after the second transition (stage IV) as shown in Fig. 3(a).

## Conclusion

Based on the excitation dose, wavelength, and temperature-controlled studies, the photoinduced phase transitions of VO<sub>2</sub> are inspected over the dynamical signatures from multiple scattering channels, including Bragg diffraction, diffusive scattering, and coherent oscillation as a probe for acoustic waves. Several new observations were made which can be correlated with earlier pump-probe and thermodynamic measurements to address the on-going questions. Firstly, we show that the ultrafast dynamics of photoinduced phase transition in VO<sub>2</sub> is density-driven and can be significantly subthermal using long wavelength photons. Secondly, we demonstrate that the phase transition involves at least two main steps with a well distinguishable intermediate state taking on a motif akin to  $M_2$ , coupling to concerted detwisting and depairing along two different V-V sublattice chains. This symmetry change is consistent with the hole-doping picture<sup>10</sup> for the initial evolution, but the extent of excess holes at the threshold level may be adequate to drive the system metallic<sup>22,24</sup>. Thirdly, we identify the unusual roles of the transient stress and their remediation through the launch of impulsive acoustic waves coupled to wavelength-dependent diffusive signatures of lattice instabilities that trigger such events. Given the decisive role of this strain relief in transitioning into the final rutile phase, one may envision using strain as a control parameter for phase transition. This may also help understand several recent accounts of unusually stable photoinduced monoclinic metal under the influence of stress<sup>33,35</sup>. Conversely, by exploiting the flexibility associated with amorphous-membrane-supported ultrafine VO<sub>2</sub> nanocrystalline systems to reduce the role of the transient stress, a relatively unhindered high speed interaction-driven switching may be established.

Regarding whether the results reported here are applicable to single-crystal systems, we first draw comparisons between the temperature-mediated and photoinduced phase transition in both single-crystal and polycrystalline systems. Previous study of VO<sub>2</sub> nanobeams gently placed (nearly stress-free) on a substrate showed extremely narrow transition width for both thermally and optically induced transitions (<0.2 K, <0.1 mJ/cm<sup>2</sup> respectively)<sup>27</sup>, whereas the phase transitions in epitaxially grown VO<sub>2</sub> sample can be broadened by up to tens of K due to the static strain induced by sample-substrate mismatch<sup>34</sup>. Meanwhile, in the nanocrystalline film reported here, the thermal transition is inhomogeneously broadened due to surface stress while experiencing lesser external stress from the substrate due to its amorphous nature. It is expected that this inhomogeneous broadening will be translated to optically driven transformation, nonetheless, we demonstrate that the difference in the thresholds observed here using two different photon wavelengths greatly exceeds the inhomogeneous widths of the respective transformations [Fig. 1(c)]. Therefore, the underlying physics of the interaction-driven transition and the emergence of transient metastable state are robust against inhomogeneity. It is interesting to point out that while the onset threshold of our experiments is found to be consistent with earlier studies using both polycrystalline and single-crystal samples<sup>16,20–22,28</sup>, the full switching threshold witnessed here is substantially lower than earlier results because of the avoidance of excessive transient stress. We expect the same processes to occur in single-crystal VO<sub>2</sub> systems, particularly when steps are taken to reduce the external constraint to avoid both static and transient stress that may serve as a feedback to influence the phase transition dynamics as described earlier. Future more sensitive experiments on isolated single-crystal nanobeams under controlled stress and excitation wavelengths should provide more information on the anisotropic phonon softening tied to the phase transition and elaborate on the mechanism responsible for the decay of the metastable phase under the influence of stress.

Finally, the findings presented here should be relevant to the development of new electronic applications. Our observations suggest that carrier doping to be the key mechanism to induce the metastable M<sub>2</sub>\* doorway state, which facilitates the ultrafast conversion of insulating M<sub>1</sub> into metallic phase, even under a subthermal scenario. It is therefore reasonable to suggest that such a channel might be active through the nonequilibrium transport studies where hot carriers could be directly injected via intense current pulse or electrostatic gating. Indeed, tantalizing evidences of nonthermal insulator-metal switching<sup>53,54</sup> operated at very high speed (~1 ns, resolution-limited) in sandwiched nanoscale VO<sub>2</sub> film has recently been reported<sup>55</sup>. Whether or not a similar pathway is involved in the electrically driven transition as in the photo-doping scenario awaits further elucidation. It would be very interesting to explore the avenue of optically assisted insulator-metal transition using lower-energy photons taking advantage of their large penetration depth in such device implementation by leveraging the carrier-driven emergent state to circumvent thermodynamic limitations for more efficient and ultrafast switching<sup>56</sup>.

## Methods

**Sample synthesis.** The VO<sub>2</sub> thin film samples used in the experiments were prepared via pulsed laser deposition<sup>57,58</sup> on 9 nm thick amorphous silicon (a-Si) 100 μm × 100 μm TEM membrane windows (SIMPore: US100-A09Q33). The TEM windows were first attached to a silicon substrate, which was then loaded into a custom-built vacuum chamber for the deposition of VO<sub>2</sub> thin films. Before the deposition started, the background pressure was lowered to 8 × 10<sup>-6</sup> Torr to remove impurity ambient gases. Upon deposition, the temperature of the sample was increased to ~550 °C, whereas the oxygen was introduced in the chamber at a constant rate of 20 standard cubic centimeters per minute (sccmm). Meanwhile, the pressure was controlled by a butterfly control valve to maintain at 15 mTorr. A krypton fluoride (KrF) excimer laser was operated at 10 Hz under a pulse energy of ~350 mJ (fluence of approximately 2 J/cm<sup>2</sup>) to ablate vanadium from a solid metallic target inside the chamber to grow VO<sub>2</sub> films on the substrate. During deposition, the sample was constantly rotated for an even distribution of heat and material deposition. Upon completion of the deposition time, the laser was turned off and the sample went through a 30 minute annealing process under the same environment conditions. Under this process, it took ~7 minutes and 30 seconds to grow ~50 nm thick films, which was confirmed by using AFM. Using a scanning electron microscope (SEM), we can differentiate the nanosized grain composition and establish a grain size distribution to be around 31 ± 7 nm, as shown in Supplementary Fig. S1.

**Characterization.** The steady-state insulator-metal transition of the as-prepared VO<sub>2</sub> thin film was confirmed by temperature-dependent resistance measurement depicted in Supplementary Fig. S2(a), showing 2 orders of magnitude change in resistance across the transition temperature  $T_C \sim 340$  K<sup>6</sup>. A dispersion of ~8 K is also identified, which we attributed to the inhomogeneity-induced broadening, rather than the intrinsic property of VO<sub>2</sub>, as evidenced in recent studies of single-crystal nanobeams<sup>27,38,59</sup>. Also shown is the structure phase transition (see Supplementary Fig. S2(b)), monitored through the electron diffraction, in which the (3, 0, -2) intensity is used as an order parameter to gauge the degree of phase transition. We note that the measured resistivity continues to change beyond the structural transition region. This trend is indicative of a continuous change in the electronic property of VO<sub>2</sub> beyond  $T_C$ , not correlated with the structural phase transition<sup>38,59</sup>.

**Ultrafast electron diffraction.** The ultrafast electron diffraction experiments were conducted using the ultrafast electron crystallography (UEC) and the ultrafast electron microdiffraction (UEmD) systems. The low temperature studies were performed in the UEC system where the sample goniometer can be cooled to 20 K<sup>5</sup>. Temperature was measured with 0.01 K precision at the back of sample holder, which was in a solid thermal contact with the sample grid, which was clamped into a copper counter sink on the sample holder. The probe size was controlled via adjusting a condenser lens in front of the sample to 30 μm in full-width-at-half-maximum (FWHM) in this experiment ensuring the electron beam was fully contained near the center of the VO<sub>2</sub> film deposited on the 100 μm × 100 μm TEM membrane window. The pump pulse was generated by an optical parametric amplifier driven by a 45 fs, 800 nm amplified laser system (Spectra Physics, Ti: Sapphire, Regenerative



Amplification), and can be tuned from 200 nm to 3000 nm in wavelength. In this experiment, primarily 800 nm and 2000 nm wavelength were used. The size of the pump beam at different wavelength was adjusted by varying the position of a focusing lens. Its size along x direction (see Supplementary Fig. S3(a)) was directly measured via knife-edge measurement *in situ*, while the aspect ratio of the pump laser spot was determined *in situ* using laser-electron cross-correlation approach (see SI). Part of the incident laser beam was also split off by a beam splitter before entering the diffraction chamber, which was monitored with a beam profiler to cross check the size and intensity of the beam during the experiment. We set the pump size to be  $\sim 400 \mu\text{m}$  in FWHM, which was significantly larger than the probe size to ensure that within the probed area the sample was homogeneously illuminated by the pump laser. The room temperature studies were also conducted using the UEmD system where the beam energy can be adjusted up to 100 keV. We determine the normalized diffraction intensity changes do not vary strongly over the beam energy. We kept the repetition rate to be  $\leq 500$  Hz to ensure there was no residual heating effect that would change the initial state. This is verified by *in situ* monitoring the diffraction patterns produced at negative timeframes to be consistent with that obtained from the sample without optical pumping, and the threshold dose at a given temperature is independent of the exposure time (see Supplementary Fig. S4).

## References

- Nasu, K. *Photoinduced phase transitions*. (World Scientific Pub. Co. Inc., 2004).
- Fausti, D. *et al.* Light-induced superconductivity in a stripe-ordered cuprate. *Science* **331**, 189–191 (2011).
- Stojchevska, L. *et al.* Ultrafast switching to a stable hidden quantum state in an electronic crystal. *Science* **344**, 177–180 (2014).
- Ichikawa, H. *et al.* Transient photoinduced ‘hidden’ phase in a manganite. *Nat. Mater.* **10**, 101–105 (2011).
- Han, T.-R. T. *et al.* Exploration of metastability and hidden phases in correlated electron crystals visualized by femtosecond optical doping and electron crystallography. *Sci. Adv.* **1**, e1400173 (2015).
- Morin, F. J. Oxides which show a metal-to-insulator transition at the neel temperature. *Phys. Rev. Lett.* **3**, 34–36 (1959).
- Whittaker, L., Patridge, C. J. & Banerjee, S. Microscopic and nanoscale perspective of the metal-insulator phase transitions of VO<sub>2</sub>: Some new twists to an old tale. *J. Phys. Chem. Lett.* **2**, 745–758 (2011).
- Eyert, V. The metal-insulator transitions of VO<sub>2</sub>: A band theoretical approach. *Ann. Phys.* **11**, 650–702 (2002).
- Wu, Y. *et al.* Depressed transition temperature of W<sub>x</sub>V<sub>1-x</sub>O<sub>2</sub>: mechanistic insights from the X-ray absorption fine structure (XAFS) spectroscopy. *Phys. Chem. Chem. Phys.* **16**, 17705 (2014).
- Pouget, J. P. *et al.* Dimerization of a linear Heisenberg chain in the insulating phases of V<sub>1-x</sub>Cr<sub>x</sub>O<sub>2</sub>. *Phys. Rev. B* **10**, 1801–1815 (1974).
- Biermann, S., Poteryaev, A., Lichtenstein, A. I. & Georges, A. Dynamical singlets and correlation-assisted peierls transition in VO<sub>2</sub>. *Phys. Rev. Lett.* **94**, 26404 (2005).
- Weber, C. *et al.* Vanadium dioxide: A peierls-mott insulator stable against disorder. *Phys. Rev. Lett.* **108**, 1–5 (2012).
- Zylbersztein, A. & Mott, N. F. Metal-insulator transition in vanadium dioxide. *Phys. Rev. B* **11**, 4383–4395 (1975).
- Goodenough, J. B. The two components of the crystallographic transition in VO<sub>2</sub>. *J. Solid State Chem.* **3**, 490–500 (1971).
- Cavalleri, A., Dekorsy, T., Chong, H. H. W., Kieffer, J. C. & Schoenlein, R. W. Evidence for a structurally-driven insulator-to-metal transition in VO<sub>2</sub>: A view from the ultrafast timescale. *Phys. Rev. B* **70**, 161102(R) (2004).
- Baum, P., Yang, D.-S. & Zewail, A. H. 4D visualization of transitional structures in phase transformations by electron diffraction. *Science* **318**, 788–792 (2007).
- Cavalleri, A. *et al.* Femtosecond structural dynamics in VO<sub>2</sub> during an ultrafast solid-solid phase transition. *Phys. Rev. Lett.* **87**, 237401 (2001).
- Cocker, T. L. *et al.* Phase diagram of the ultrafast photoinduced insulator-metal transition in vanadium dioxide. *Phys. Rev. B* **85**, 155120 (2012).
- Hilton, D. J. *et al.* Enhanced photosusceptibility near T<sub>c</sub> for the light-induced insulator-to-metal phase transition in vanadium dioxide. *Phys. Rev. Lett.* **99**, 226401 (2007).
- Kübler, C. *et al.* Coherent structural dynamics and electronic correlations during an ultrafast insulator-to-metal phase transition in VO<sub>2</sub>. *Phys. Rev. Lett.* **99**, 116401 (2007).
- Pashkin, A. *et al.* Ultrafast insulator-metal phase transition in VO<sub>2</sub> studied by multiterahertz spectroscopy. *Phys. Rev. B* **83**, 1–9 (2011).
- Wegkamp, D. *et al.* Instantaneous band gap collapse in photoexcited monoclinic VO<sub>2</sub> due to photocarrier doping. *Phys. Rev. Lett.* **113**, 2–6 (2014).
- Becker, M. F. *et al.* Femtosecond laser excitation of the semiconductor-metal phase transition in VO<sub>2</sub>. *Appl. Phys. Lett.* **65**, 1507–1509 (1994).
- Rini, M. *et al.* Optical switching in VO<sub>2</sub> films by below-gap excitation. *Appl. Phys. Lett.* **92**, 181904 (2008).
- Cavalleri, A. *et al.* Band-selective measurements of electron dynamics in VO<sub>2</sub> using femtosecond near-edge X-ray absorption. *Phys. Rev. Lett.* **95**, 67405 (2005).
- Tao, Z., Han, T. R. T. & Ruan, C. Y. Anisotropic electron-phonon coupling investigated by ultrafast electron crystallography: Three-temperature model. *Phys. Rev. B* **87**, 235124 (2013).
- Tao, Z. *et al.* Decoupling of structural and electronic phase transitions in VO<sub>2</sub>. *Phys. Rev. Lett.* **109**, 166406 (2012).
- Morrison, V. R. *et al.* A photoinduced metal-like phase of monoclinic VO<sub>2</sub> revealed by ultrafast electron diffraction. *Science* **346**, 445–448 (2014).
- Zeiger, H. J. *et al.* Theory for displacive excitation of coherent phonons. *Phys. Rev. B* **45**, 768–778 (1992).
- Wall, S. *et al.* Ultrafast changes in lattice symmetry probed by coherent phonons. *Nat. Commun.* **3**, 721 (2012).
- O’Callahan, B. T. *et al.* Inhomogeneity of the ultrafast insulator-to-metal transition dynamics of VO<sub>2</sub>. *Nat. Commun.* **6**, 6849 (2015).
- Kim, H.-T. *et al.* Monoclinic and correlated metal phase in VO<sub>2</sub> as evidence of the mott transition: Coherent phonon analysis. *Phys. Rev. Lett.* **97**, 266401 (2006).
- Laverock, J. *et al.* Direct observation of decoupled structural and electronic transitions and an ambient pressure monoclinic metallic phase of VO<sub>2</sub>. *Phys. Rev. Lett.* **113**, 216402 (2014).
- Liu, M. K. *et al.* Anisotropic electronic state via spontaneous phase separation in strained vanadium dioxide films. *Phys. Rev. Lett.* **111**, 96602 (2013).
- Hsieh, W.-P. *et al.* Evidence for photo-induced monoclinic metallic VO<sub>2</sub> under high pressure. *Appl. Phys. Lett.* **104**, 21917 (2014).
- Sciaimi, G. & Miller, R. J. D. Femtosecond electron diffraction: heralding the era of atomically resolved dynamics. *Reports Prog. Phys.* **74**, 96101 (2011).
- Ischenko, A. & Aseyev, S. A. Eds. Time-resolved electron diffraction: For chemistry, biology and materials science, in *Advances in Imaging and Electron Physics*. **184**, <http://www.sciencedirect.com/science/article/pii/B9780128001455210010> (Elsevier, 2014).
- Wei, J., Wang, Z., Chen, W. & Cobden, D. H. New aspects of the metal-insulator transition in single-domain vanadium dioxide nanobeams. *Nat. Nanotechnol.* **4**, 420–424 (2009).
- Marezio, M., McWhan, D. B., Remeika, J. P. & Dernier, P. D. Structural aspects of the metal-insulator transitions in Cr-doped VO<sub>2</sub>. *Phys. Rev. B* **5**, 2541–2551 (1972).

40. Longo, J. M. & Kierkegaard, P. A refinement of the structure of VO<sub>2</sub>. *Acta Chem. Scand.* **24**, 420–426 (1970).
41. Kucharczyk, D. & Niklewski, T. Accurate X-ray determination of the lattice parameters and the thermal expansion coefficients of VO<sub>2</sub> near the transition temperature. *J. Appl. Crystallogr.* **12**, 370–373 (1979).
42. Berglund, C. N. & Guggenheim, H. J. Electronic properties of VO<sub>2</sub> near the semiconductor-metal transition. *Phys. Rev.* **185**, 1022–1033 (1969).
43. Budai, J. D. *et al.* Metallization of vanadium dioxide driven by large phonon entropy. *Nature* **515**, 535–539 (2014).
44. Koethe, T. C. *et al.* Transfer of spectral weight and symmetry across the metal-insulator transition in VO<sub>2</sub>. *Phys. Rev. Lett.* **97**, 116402 (2006).
45. Verleur, H. W., Barker, A. S. & Berglund, C. N. Optical properties of VO<sub>2</sub> between 0.25 and 5 eV. *Rev. Mod. Phys.* **40**, 737 (1968).
46. Guinier, A. *X-ray diffraction in crystals, imperfect crystals, and amorphous bodies*. (Dover Publications, 1994).
47. Ruan, C.-Y. *et al.* The development and applications of ultrafast electron nanocrystallography. *Microsc. Microanal.* **15**, 323–337 (2009).
48. Farrow, C. L., Ruan, C. Y. & Billinge, S. J. L. Quantitative nanoparticle structures from electron crystallography data. *Phys. Rev. B* **81**, 134104 (2010).
49. He, Z. & Millis, A. J. Photoinduced phase transitions in narrow-gap Mott insulators: The case of VO<sub>2</sub>. *Phys. Rev. B* **93**, 115126 (2016).
50. Yuan, X., Zhang, W. & Zhang, P. Hole-lattice coupling and photoinduced insulator-metal transition in VO<sub>2</sub>. *Phys. Rev. B* **88**, 35119 (2013).
51. Haverkort, M. W. *et al.* Orbital-assisted metal-insulator transition in VO<sub>2</sub>. *Phys. Rev. Lett.* **95**, 196404 (2005).
52. Maurer, D., Leue, A., Heichele, R. & Müller, V. Elastic behavior near the metal-insulator transition of VO<sub>2</sub>. *Phys. Rev. B* **60**, 13249–13252 (1999).
53. Stabile, A. a. *et al.* Separating electric field and thermal effects across the metal-insulator transition in vanadium oxide nanobeams. *Appl. Phys. Lett.* **107**, 13503 (2015).
54. Wu, B. *et al.* Electric-field-driven phase transition in vanadium dioxide. *Phys. Rev. B* **84**, 241410(R) (2011).
55. Zhou, Y. *et al.* Voltage-triggered ultrafast phase transition in vanadium dioxide switches. *IEEE Electron Device Lett.* **34**, 220–222 (2013).
56. Zhou, Y. & Ramanathan, S. Correlated electron materials and field effect transistors for logic : A review. *Crit. Rev. Solid State Mater. Sci.* **38** (2013).
57. Rúa, A., Fernández, F. E. & Sepúlveda, N. Bending in VO<sub>2</sub>-coated microcantilevers suitable for thermally activated actuators. *J. Appl. Phys.* **107**, 74506 (2010).
58. Cabrera, R., Merced, E. & Sepúlveda, N. A micro-electro-mechanical memory based on the structural phase transition of VO<sub>2</sub>. *Phys. Status Solidi A* **9**, 1704–1711 (2013).
59. Cao, J. *et al.* Strain engineering and one-dimensional organization of metal-insulator domains in single-crystal vanadium dioxide beams. *Nat. Nanotechnol.* **4**, 732–737 (2009).

## Acknowledgements

The authors acknowledge S.B. Mahanti, P.M. Duxbury, and J. McGuire for useful discussions, and R. Loloee and B. Bi for assistance in preparing and characterizing the VO<sub>2</sub> films. The work was funded by DOE grant DE-FG02-06ER46309 and supported by NSF MRI facility grant DMR 1126343.

## Author Contributions

C.-Y.R. and Z.T. conceived the experiments. Z.T., F.Z., T.-R.T.H., K.C. and C.-Y. R performed the ultrafast diffraction and microscopy measurements. M.Y. and R.R.L. performed the optical measurements. D.T., T.W. and N.S. prepared the samples. Z.T., F.Z., T.-R.T.H. and C.-Y.R. did the analyses. C.-Y.R. and Z.T. wrote the paper. All authors reviewed the manuscript.

## Additional Information

**Supplementary information** accompanies this paper at <http://www.nature.com/srep>

**Competing financial interests:** The authors declare no competing financial interests.

**How to cite this article:** Tao, Z. *et al.* The nature of photoinduced phase transition and metastable states in vanadium dioxide. *Sci. Rep.* **6**, 38514; doi: 10.1038/srep38514 (2016).

**Publisher's note:** Springer Nature remains neutral with regard to jurisdictional claims in published maps and institutional affiliations.



This work is licensed under a Creative Commons Attribution 4.0 International License. The images or other third party material in this article are included in the article's Creative Commons license, unless indicated otherwise in the credit line; if the material is not included under the Creative Commons license, users will need to obtain permission from the license holder to reproduce the material. To view a copy of this license, visit <http://creativecommons.org/licenses/by/4.0/>

© The Author(s) 2016